The International Journal of Advanced Manufacturing Technology (2024) 134:2815–2832
https://doi.org/10.1007/s00170-024-14297-x

ORIGINAL ARTICLE

Analyzing the effect of infill density on the mechanical compression of ASA in additive manufacturing: a FEM perspective

Nikolaos E. Karkalos[1] · **Kacper Rydzoń**[2] · **Emmanouil L. Papazoglou**[1] · **Panagiotis Karmiris-Obratański**[1,2]

Received: 18 February 2024 / Accepted: 14 August 2024 / Published online: 26 August 2024

Abstract

Additive manufacturing (AM) represents a novel method for parts manufacturing, revolutionizing the design principles and processes. Among the different AM methods, fused filament fabrication (FFF) is one of the most widely employed and affordable, with numerous applications across a broad range of fields. Inherently, due to the fundamental physical mechanisms occurring during part building, the material acquires different properties compared to those of bulk material. Simultaneously, parameters such as the infill pattern and infill density significantly affect the overall behavior of the part. An efficient and effective tool to minimize the necessity for experimental investigations and to define the mechanical properties with respect to these parameters (i.e., infill density and pattern) is the finite element method (FEM). In the current study, accurate FEM models were developed and presented, considering the precise geometry of compression specimens for simulating the compression behavior of FFF-printed ASA polymer. More specifically, honeycomb infill patterns with different infill densities were simulated, and the results were validated by direct comparison to respective experimental results. It was deduced that utilizing an appropriate mesh size leads to higher precision and also increases the stability of the numerical simulation, while the FEM models can predict the loads as well as the deformed geometric shapes for different infill densities. As an overall conclusion, it is proved and reasoned that employing FEM and a proper modeling approach is indeed a feasible and efficient way to predict and define the compressive behavior of FFF parts.

Keywords FFF · FEM · Compression · Mechanical properties · Hexagon · Meshing sensitivity

1 Introduction

Over the last few decades, additive manufacturing (AM) has become a novel alternative in the manufacturing sector, introducing a unique approach to producing mechanical components along with various benefits. Continuous research is being conducted to enhance the printing processes for diverse materials, including metals, ceramics, polymers, and composites [1, 2]. A key benefit of the AM process is its ability to fabricate parts with intricate shapes and varied densities, thereby minimizing material usage without sacrificing the strength and integrity of these components [3]. Particularly for polymer-based parts, there is an emphasis on balancing the advantage of lightness with the requisite mechanical robustness to make them suitable for more challenging applications [4]. Commonly, processes like fused filament fabrication (FFF), selective laser sintering (SLS), and stereolithography (SLA) are preferred for the reliable construction of these polymer components [5].

During the printing phase, the internal configuration of the parts is crucial for maintaining mechanical properties, reducing weight, and minimizing printing time [6]. This involves a strategic choice between opting for a fully dense infill, which, although resource-intensive in terms of material consumption and fabrication time, thereby increasing the cost, ensures superior mechanical robustness. Alternatively, employing infill patterns (IP) can replicate specific mechanical attributes while enhancing the part's overall lightness [7, 8]. IP, integral to the optimization of strength within additive manufacturing, denote the internal lattice or grid-like

✉ Panagiotis Karmiris-Obratański
karmiris@agh.edu.pl

[1] Laboratory of Manufacturing Technology, School of Mechanical Engineering, National Technical University of Athens, 15780 Athens, Greece

[2] Advanced Manufacturing Laboratory, Department of Manufacturing Systems, Faculty of Mechanical Engineering and Robotics, AGH University of Krakow, 30-059 Krakow, Poland

structures within a 3D-printed component. The selection from a diverse array of available infill geometries, each imparting unique mechanical characteristics such as stiffness and tensile strength, is crucial [9]. The challenge lies in identifying the most appropriate pattern that aligns with the desired mechanical properties and application-specific requirements. A suboptimal choice in infill configuration can lead to inefficiencies in material usage, extended production timelines, and potentially compromised functional performance of the final printed part [10, 11].

To accurately evaluate the mechanical integrity of components fabricated via additive manufacturing techniques, it is imperative to conduct extensive experimental investigations. These investigations are aimed at elucidating the relationship between the inherent material properties and an array of process-specific parameters [12, 13]. In the scientific literature, there has been substantial research dedicated to ascertaining the mechanical attributes of polymers processed through AM modalities [14]. Lubombo and Huneault [8] investigated the effect of 3D printed PLA infill patterns on the mechanical properties. They found that by simply altering the IP or increasing the number of perimeter shells while maintaining the same density, the material's stiffness doubled and its strength increased by up to 82% and 84%, respectively. In the work of Forés-Garriga et al. [15], it was investigated the role of the IP on the weight reduction and mechanical properties of PEI ultem vi FFF. The results analysis establishes a relationship between the infill configuration and mechanical performance, taking into account both intra-layer and inter-layer bonding. A 3D waiving IP was investigated by Yao et al. [16]. According to their findings, when compared to parts produced by layer-to-layer deposition in 3D weaving, the anisotropy within the layers' mechanical properties is notably reduced, dropping to 10.21% and 0.98%. LaleganiDezaki and MohdAriffin [17] investigated the effect of combined IP on the mechanical properties of FFF parts. Additionally, samples built at 0° orientation, both in the flat and on-edge directions, exhibited the strongest layer adhesion and highest quality. Conversely, samples built at perpendicular orientations, such as 60° and 75°, demonstrated weaker adhesion and were the most fragile in both flat and on-edge orientations. In summary, the study found that increasing the build orientation angle leads to a decrease in strength.

The rapid evolution of 3D printing technologies has necessitated the integration of advanced simulation tools to optimize design and manufacturing processes. Among these tools, finite element analysis (FEA) stands out due to its capability to accurately model and analyze complex geometrical structures [18, 19]. Mercado-Colmenero et al. [20] presented a combined numerical and experimental investigation into the uniaxial compression properties of PLA (polylactic acid) manufactured using FFF technology, specifically focusing on product specifications. The results demonstrate that the model, which applies a polynomial function, closely aligns with experimental outcomes, displaying a minimal error of only 0.36%, in contrast to the previous model that used a constant Young's compression modulus and exhibited a significantly higher error of 4.27%. Using FEM, Forés-Garriga et al. [21] investigated the mechanical response of AM cell patterns and the influence of cell density on printing time and compression strength. The authors have conducted a detailed analysis of the excellent elastic performance of Sparse infill and derived analytical expressions to calculate the elastic moduli in three orthogonal directions. Using fluid-filled structures, Soe et al. [22] performed experimental and FEA studies on the dynamic compression behavior of FFF parts. One part was produced completely hollow, containing only air, while another was 70% filled with water, up to half its height, and a third was entirely filled with water. The findings indicate that closed-cell AM structures filled with fluid may reduce acceleration upon impact. Additionally, SPH and fluid-based air-cavity computational techniques were effectively used for simulating water and air, respectively [23]. Gonabadi et al. [24] explored the impact of raster angle, build orientation, and infill density (ID) on the elastic behavior of 3D printed components through finite element microstructural modeling and homogenization FEM methods. The authors found that by using FEM, they were able to predict the elastic properties, although there is a need to develop more advanced models for samples with IP [25]. An experimental and numerical investigation on the influence of vertical strut configurations on the compressive behavior of 3D printed polymer lattice structures was investigated by Fadeel et al. [26]. Both experimental findings and finite element modeling indicate that the presence of vertical struts enhances the strength of lattice structures, with the specific energy absorption (SEA) being dependent on the lattice geometry rather than its mass. Finally, Hmeidat et al. [27] examined experimentally and by fine element analysis, how IP affect the strength and stiffness of 3D printed topologically optimized geometries. The study utilizes a benchmark topology optimization problem and fused filament fabrication to evaluate how different infill patterns affect the strength, stiffness, and failure behavior of 3D printed structures. The results show that the choice of IP leads to notable differences in the stiffness and failure load of the printed objects. This highlights the crucial role of selecting appropriate infill patterns in the design process to achieve optimal performance in 3D printed structures.

The literature review highlights that, although there are studies relevant to the mechanical behavior of solid 3D printed and lattice structures, to the best of the authors' knowledge, there is a lack of studies integrating FEM and experimental analysis on the compression of samples with different infill density values, printed using FFF. For that reason, a comprehensive experimental and numerical work was carried out, by studying the effect of infill density on the compression behavior of polymer specimens in a wide range of infill density values, spanning from 0% (specimen with top and bottom surfaces as well as walls) to 80%. The results indicate that the adopted FE approach provides highly accurate results, especially for infill density values up to 65%, and can be efficiently used as a reliable tool for the prediction of the mechanical behavior of printed parts.

1.1 Literature review

In order to prove the necessity and importance of the current work, a concise review of the relevant literature was performed. Various authors have carried out studies based on FE models in order to predict the mechanical behavior of FFF-printed specimens. Based on the work of Paul [28], only a small amount of works have been carried out regarding FE modeling of FDM compared to other processes, mostly on mechanical properties characterization, and even these models often lack realistic features. The existing works can be categorized into works which model the properties of printed parts indirectly (either by a simplified geometric model or by micromechanical model), works which model lattice structures and works which model the internal structure of the printed specimens explicitly by taking into account the infill pattern, infill density, and wall thickness, such as the model which is presented in this work. As our work focuses on the compressive behavior of printed specimens, most of the works which will be discussed are relevant to the compression test of FFF-printed specimens.

Regarding the first category of models, Torre et al. [29] conducted FE numerical simulations for the compressive behavior of PLA in which the material was modeled as elastoplastic isotropic material based on experimental results. Mercado-Colmenero et al. [30] used an elastic model for the simulation of FFF-printed parts, based on experimental results about material properties. Mercado-Colmenero et al. [31] also simulated a special structure of a printed construction element using a linear isotropic elastic model. Athale et al. [32] modeled the 3D printed material by an orthotropic elastic-anisotropic plastic material. Bandinelli et al. [33] also took into consideration the anisotropy of printed material properties for their FE model of PA12-CFRP composites compression. Garcia-Granada [34] carried out simulations for compression of printed specimens under dynamic loading and compared the use of a foam constitutive model and an elasto-plastic one, created based on experimental results. Kerekes et al. [35] adopted the Gurson-Tvergaard model for the mechanical behavior of the printed specimens, which was fitted based on the experimental results. Bhandari et al. [36] created a special bimodular elasto-plastic material for FE simulations of FFF-printed parts, including different properties for tensile and compressive behavior. The part was modeled as a shell with stacked layers of orthotropic laminae for which the mechanical behavior was determined by laminate analysis. Pastor-Artigues et al. [37] also raised the issue of bimodular behavior of printed PLA specimens, indicating that a modified constitutive model is required to model their behavior by numerical models.

Apart from the works in which the FFF-printed material is modeled by a specific material model, there are a few works which focus on the use of micromechanical models, whose characteristics are extensively discussed in the work of Bol and Šavija [38]. For example, Gonabadi et al. [39] developed an RVE model to study the micromechanical behavior of FFF-printed specimens with interbead voids. Using the RVE model and homogenized properties, they simulated cases with different layer height, layer width, and overlap and determined the response of the specimens in each case.

Another category of FE simulations of the mechanical behavior of FFF-printed parts is related to lattice structures. Lattice structures are usually open-cell structures with a special geometry, aiming for improved mechanical behavior. In the relevant literature, a wide range of lattice structures were simulated, such as BCC [40, 41], BCC-Z [42, 43], cubic [44], honeycomb [44–49], bioinspired, such as bamboo [44, 47] or other structures [47, 50], gyroid [51], and auxetic geometries [48, 49]. In these studies, the exact geometry of the lattice was explicitly modeled, whereas the material model was usually elasto-plastic [44, 45, 47, 49, 51], isotropic-hardening plastic [40, 41], or based on the experimental stress–strain curves [42, 43, 50].

However, as it was aforementioned, additional features of FFF-printed parts, which directly affect their mechanical behavior, were not captured in these simulations, such as the walls, bottom, and top layers, as the lattice structures in these simulations are not considered to be part of the internal structure of a specimen. Thus, a third category of models exists, in which geometric models of the exact internal geometry of specimens are used. In the relevant literature, it can be seen that the research conducted, especially on compressive behavior of printed parts with detailed geometrical models, is rather limited. Podroužek et al. [52] carried out experimental and numerical studies on different 3D infill patterns such as gyroid, Schwarz D, and Schwarz P using an exact geometric model of the specimens and a non-linear material model based on the experimental stress–strain relationships. Sunny et al. [53] developed a special model for printed structures with specific infill patterns, in which they took into consideration the exact infill pattern geometry and density, whereas the effect of entrapped gas in the cavities was also modeled. Sukindar et al. [54] also created exact geometric models for compressive specimens using three different infill patterns and three different infill density values, from 30 to 70%. Finally, Guessasma et al. [55] adopted a different methodology in order to take into account the internal structure of printed specimens, by varying the Young's modulus appropriately in the computational domain so that the differences in stiffness due to overlapping filaments or voids and other weak points could be included in the model. From the literature review, it can be concluded that there is a rather limited amount of works conducted in the specific topic, and especially, a comprehensive study of the effect of infill density on the specimen strength has not yet been carried out. Thus, the present work can be proved important in this scientific field as it can clarify the evolution of mechanical behavior for a wide range of infill densities and be later used as a reference for future studies based on different infill patterns or other process parameters' values.

2 Materials and methods

2.1 Experimental study

In this study, we conducted compression tests on acrylonitrile styrene acrylate (ASA) samples, which were produced using FFF with varying infill densities and patterns. As a copolymer, ASA combines three distinct monomers, each contributing specific properties to the material. Acrylonitrile (C3H3N) provides chemical resistance and thermal stability [56], styrene (C8H8) enhances the polymer's rigidity and processability [57], and acrylate, typically butyl acrylate, significantly improves the weather resistance and impact strength [58]. Specifically, we created compressive test specimens measuring 12.7 mm in diameter and 25.4 mm in height, in line with the ASTM D695-15 standard [59]. In the compression tests, the displacement rate was 5 mm/min. Given that this displacement rate value is usually considered to be related to quasi-static conditions, it is not necessary to adopt a transient model, especially with an explicit solver, as it will be later explained in the next subsection. These specimens were designed with infill densities of 20%, 50%, and 80% and featured two distinct IPs: honeycomb (hexagonal) and gyroid. For each set of conditions, we fabricated five identical samples following the prescribed standard, orienting them vertically during printing. Additional printing parameters are detailed in Table 1, while Fig. 1 illustrates the specific IPs used in the printed samples. In order to further prove the reliability of the numerical model, a second series of experiments was carried out with infill density values of 0%, 35%, and 65%, and the results were subsequently analyzed and discussed.

Table 1 FFF process parameters' values

Parameter	Value
Printing speed [mm/s]	60
Layer height [mm]	0.18
Printing temperature [°C]	245
Platform temperature [°C]	115
Wall thickness [mm]	1.2

2.2 Numerical model details

In this study, it is intended to create a realistic model for the simulation of the behavior of the FFF-printed specimen under compressive loading. Thus, special attention is paid on different aspects of the numerical model which can guarantee the accurate representation of the compression test procedure. The simulations were carried out in ANSYS Workbench 2023 R2 software.

At first, regarding the geometry of the model, the exact geometry of the compression test specimen should be created. An important consideration for creating the actual geometry is to take into account the geometry of the actual printed specimen based on the relevant ISO standard, which is produced after the slicing procedure and is not 100% solid. As in the current work, three different infill density percentages were selected, and three separate models were developed, as can be seen in Fig. 1. Thus, the main modeling idea is to treat the specimen as a part with the properties of the solid material but with the exact printed geometry, in contrast to other studies which include a plain cylindrical geometry with experimentally derived material properties taking into consideration the infill density.

All cases which are considered in the present work are based on the hexagonal or honeycomb IP, and also, the wall thickness of the specimen is taken into account, based on the data obtained from the slicer software for the FFF process, as can be seen in Fig. 1.

The full computational model is depicted in Fig. 2, including the test specimen, as well as the two plates representing the actual platens of the testing machine. In order to reduce the simulation cost given the fact that the model is axisymmetric, only half of the compressive specimen and the upper and lower plates will be modeled. The two plates are simplified to two square-shaped plates, with a side length of 20 mm and a thickness of 1 mm.

Regarding material modeling, as can be seen in Fig. 3, apart from the ASA compressive sample, the plates are modeled as rigid material with properties equivalent to structural steel, available in the software database. ASA is modeled as an elastic–plastic material with the plasticity taken into account by a nonlinear isotropic hardening power law, which is presented in Eq. 1:

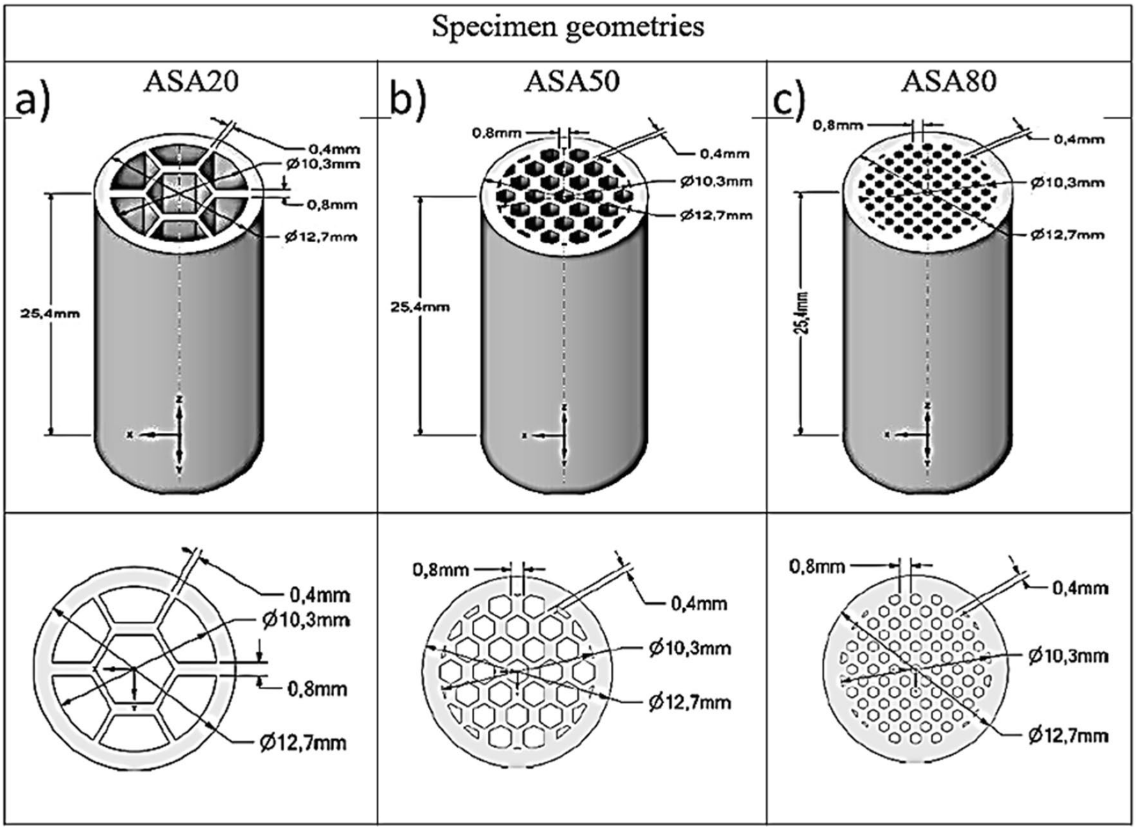

Fig. 1 Test specimen geometry used in the computational model for each case: **a** 20% infill density, **b** 50% infill density, **c** 80% infill density

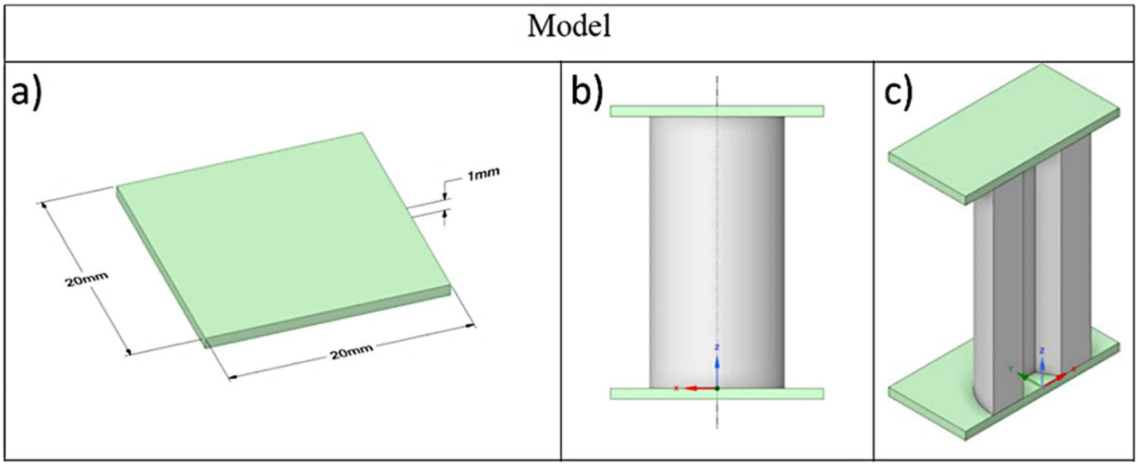

Fig. 2 The geometry of the computational model: **a** geometry of the upper and lower plate, **b** side view of the model, **c** the actual symmetric model used in the simulations

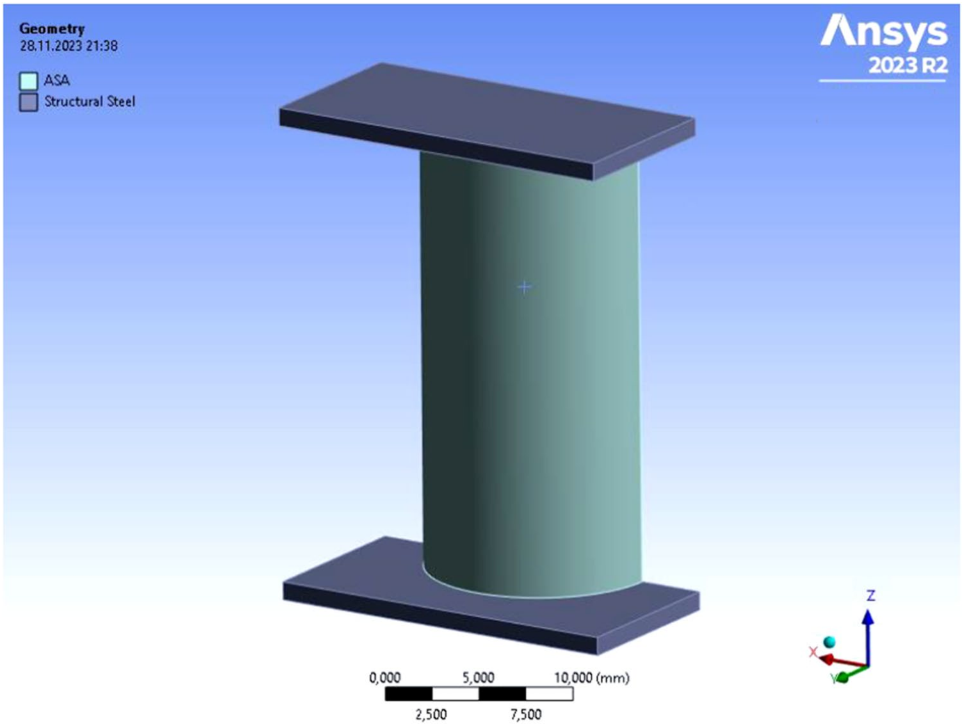

Fig. 3 Materials assigned to different parts of the model

$$\frac{\sigma_Y}{\sigma_0} = \left(\frac{\sigma_Y}{\sigma_0} + \frac{3G}{\sigma_0}\varepsilon^{pl}\right)^N \tag{1}$$

where σ_Y represents the current yield stress, σ_0 represents the initial yield stress, G is the shear modulus, ε^{pl} is the accumulated equivalent plastic strain, and N is the hardening exponent.

The data for this material model were obtained from the relevant literature, as well as material databases (MATWEB) [21].

The boundary conditions of the model are mainly applied on the upper and lower plates, as can be seen in Fig. 4. A displacement boundary condition is applied on the upper plate in order to simulate its actual gradual movement during the compression test, and a fixed support boundary condition is applied on the bottom surface of the lower plate in order to restrict its movement, as it occurs also during the actual experiment. The contact between the rigid plates and the deformable compressive specimen is assumed to be frictional with friction coefficient value of 0.1. The compressive test specimen is selected as contact body and the two plates as target bodies. Moreover, a frictional contact is defined for the test specimen, as it is expected that due to the deformation, a self-contact condition may occur.

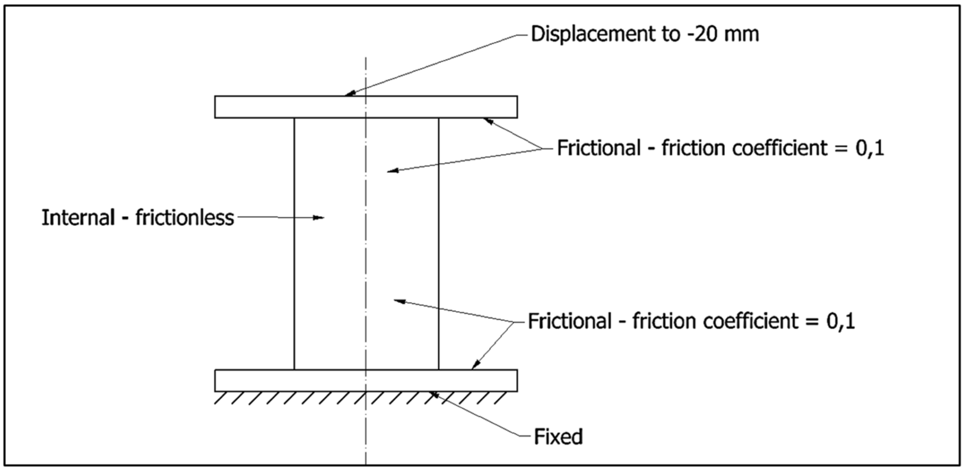

Fig. 4 Boundary and contact conditions of the computational model

The computational mesh used for the simulations included 3D solid elements, both 20-node hexahedral (Hex20) and 15-node prismatic (Wedge15 wedge elements). The length of the elements was 0.5 mm in the first two cases, whereas it was 0.6 mm for the case of 80% infill density, as it was determined by the mesh independence study which will be presented in Section 3.1.

An important consideration was also the choice of the suitable solver for the model, which could be a static structural, transient structural, or explicit dynamic structural one. Based on preliminary simulations, it was shown that the use of static or transient structural simulation did not provide considerable difference and also the use of explicit dynamics was not necessary given that the mechanical tests are conducted under quasi-static conditions, with relatively low crosshair speeds (namely 5 mm/min), so that the use of an explicit dynamics model with element deletion would lead to higher complexity of the model without a definite improvement of its accuracy, as additional parameters would be required to be determined. Thus, a static structural solver was employed with the option to take into account large deformations by recalculating the structure stiffness, as it is expected that large deformation will occur in several regions of the model. In Section 3.1, the accuracy and stability of the solver will be further discussed.

3 Results and discussion

Following the completion of simulations based on three distinct experimental cases, force-extension curves and deformation outcomes for the compressive test specimen were obtained. In this section, the findings of the mesh independence study for each model will be initially presented, subsequently followed by a detailed examination and discussion of the simulation results.

3.1 Mesh independence study

The initial step in the simulation process was to create an optimal mesh that balances mesh quality and computational efficiency in order to use the computational resources more effectively while ensuring the reliability and accuracy of the results. To achieve this, the element mesh size was varied within a reasonable range, and a thorough mesh independence study for each of the three models was conducted, which featured different test specimen geometries. The effect of the size on the simulation results was investigated in a carefully selected range in order to provide a meaningful comparison.

For the model with an infill density of 20%, the results of the mesh independence study evaluated by the force-extension curve are presented in Fig. 5. The variation of the results obtained by meshes of different sizes is not considerably high but noticeable. Apart from the accuracy of the results, there is another important reason for selecting an appropriate mesh, as it is proven that the use of coarser meshes leads to higher instabilities of the numerical solution and finally the simulation is aborted much earlier than the desired displacement value due to issues such as high local deformation of elements. On the other hand, the use of a finer mesh can ensure the stable completion of the simulation in order to achieve a result comparable to the experimental one, but a too-fine mesh increases the computational time. More specifically, based on the results of Fig. 5, it can be seen that although in some cases, a coarse mesh (with a size of 0.9 mm) can lead to relative stable simulations, higher stability can be mainly achieved when the mesh size is below 0.6 mm, and especially with a mesh size of 0.5 mm, it is possible to simulate the compression test with an extension value up to 16 mm.

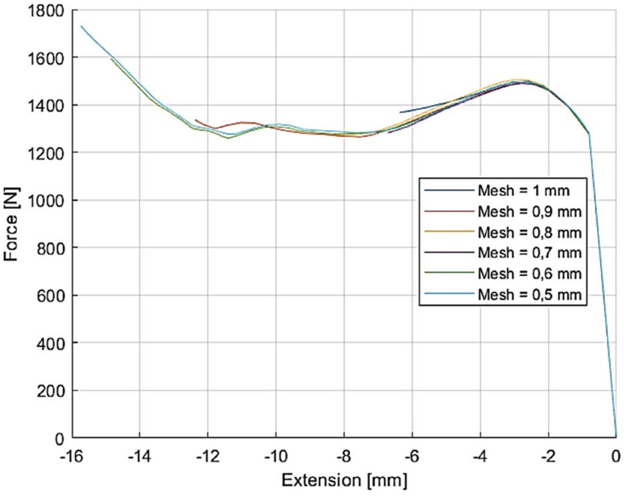

Fig. 5 Force-extension curve from mesh independence study simulations for 20% infill density

As can be directly seen in Fig. 6, the element quality of the selected mesh is sufficiently high, with most elements having a quality of 0.85 and higher (with 1.0 being the optimum value).

In the case of the model with 50% infill density, as can be seen in Fig. 7, the mesh independence study results also indicate that the use of coarse meshes not only reduces the accuracy of the model but is also related to stability issues, as the model with element size 1 mm becomes unstable before the extension reaches the value of 10 mm, whereas models with a finer mesh can eventually be stable up to 12, 13, and 14 mm, especially in the case of mesh size of 0.5 mm.

As can be seen in Fig. 8, the element quality of the selected mesh is rather high, with most elements having a

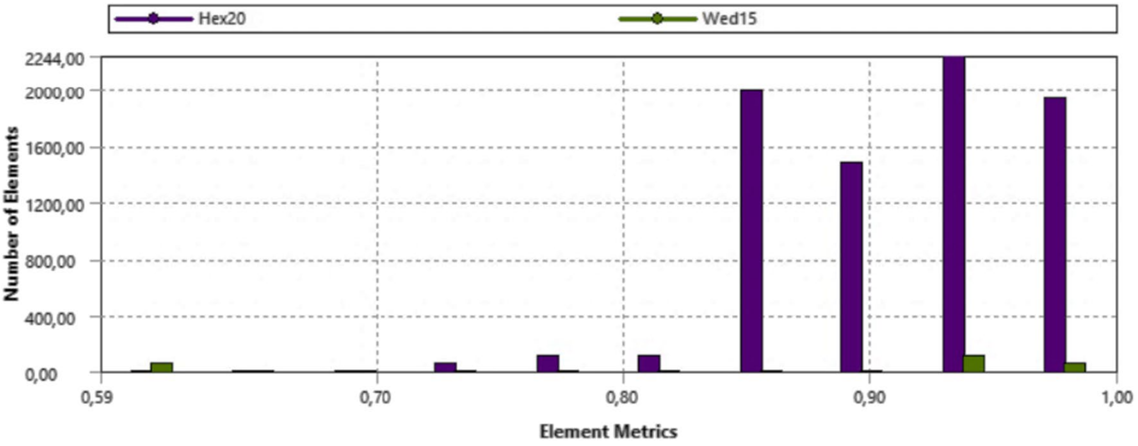

Fig. 6 Mesh quality for the model of 20% infill density

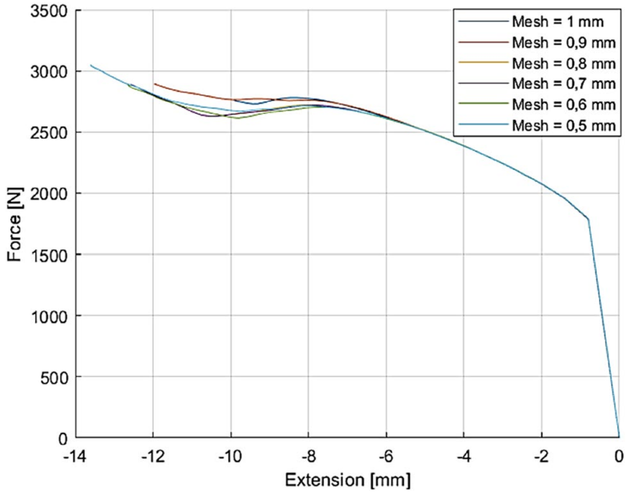

Fig. 7 Force-extension curve from mesh independence study simulations for 50% infill density

quality of 0.9 and higher, something that proves the capabilities of the developed model.

In the case of the model with 80% infill density, as can be seen in Fig. 9, probably due to the higher resemblance to a totally solid model and the considerably lower amount of voids, the results of the mesh independence study show that most of the models are stable for extension values over 15 mm and the finest model can reach up to 16 mm. The selected mesh size was 0.6 mm, as further reduction of the mesh size did not lead to a considerable difference of the results.

As can be seen in Fig. 10, the quality of the elements of the mesh is relatively high, with most elements having a quality between 0.7 and 0.88. The reason for the lower quality of elements in comparison to the two previous cases can be mainly attributed to the more complex geometry of the model, as it includes multiple small voids, with the corresponding elements having a less ideal shape. However, it is

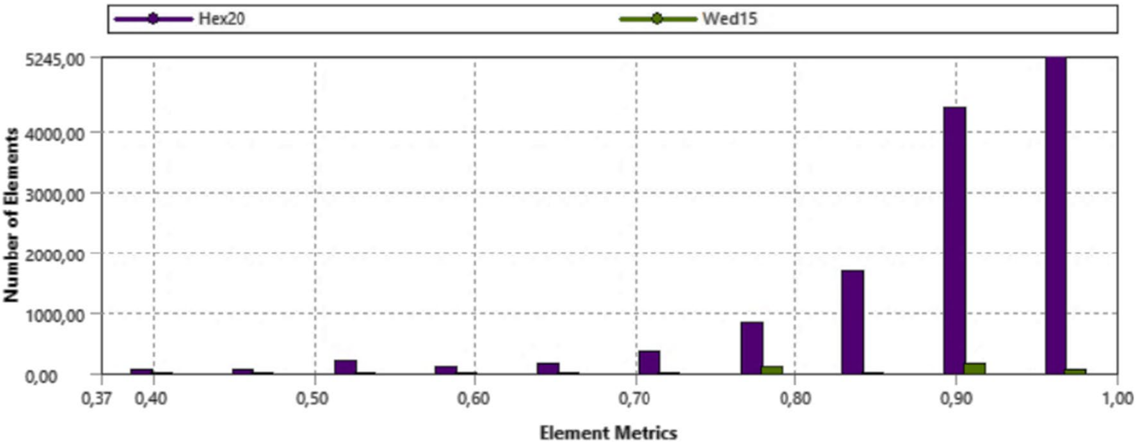

Fig. 8 Mesh quality for the model of 50% infill density

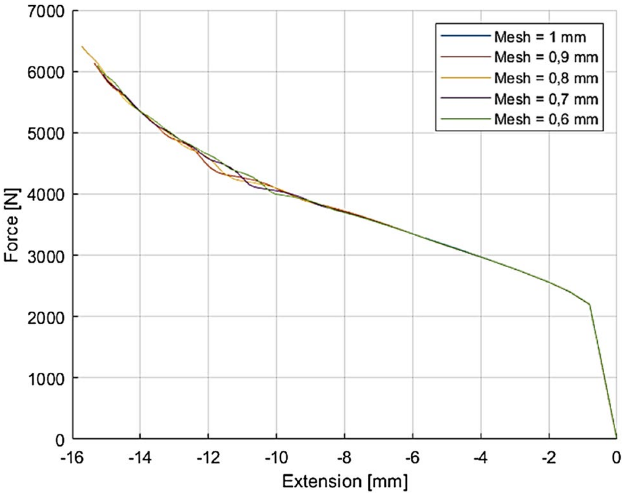

Fig. 9 Force-extension curve from mesh independence study simulations for 80% infill density

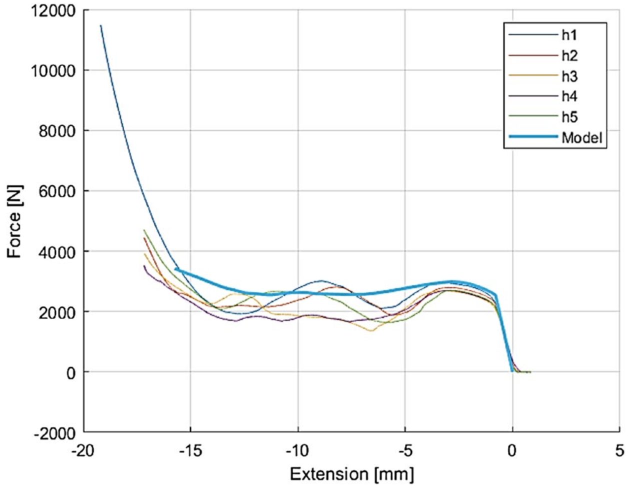

Fig. 11 Comparison of simulation and experimental results regarding the force-extension curve

not expected that the accuracy of the results will be compromised, as the use of a finer mesh did not show a considerable difference of the obtained results.

3.2 Simulations results

After the appropriate mesh was chosen for the three different cases, the respective simulations were carried out and the results were evaluated based on the predicted force–displacement curves as well as the deformed shape of the specimens which were directly compared to the experimental ones in order to verify the accuracy of the proposed model.

In the case of the specimen with 20% infill density of ASA material, in Fig. 11, the predicted force–displacement curve is present and compared to the experimental curves. As five repetitions were performed for each test based on the respective standard, it was considered important to depict all the obtained curves in the same graph in order to take into account the variation of mechanical properties during the comparison. The accuracy of the results in this case justified the fact that the proposed model can be regarded as rather promising, as the shape of the predicted force–displacement curve and its values are considerably close to the experimental ones. Initially, the first part of the curve, corresponding to the elastic deformation and the beginning of yield, is almost identical to that of the experimental curves, with a slight increase in error for displacement values around 4 mm. Then, in the region with displacement values in the range of 7–12, the predicted curve lies between the experimental ones, and finally, the curve is close to the curve corresponding to the first experiment, which shows slightly higher force values. In conclusion, in the case with 20% infill density, a sufficient degree of accuracy can be noted both for the shape of the curve, corresponding to critical stages of the

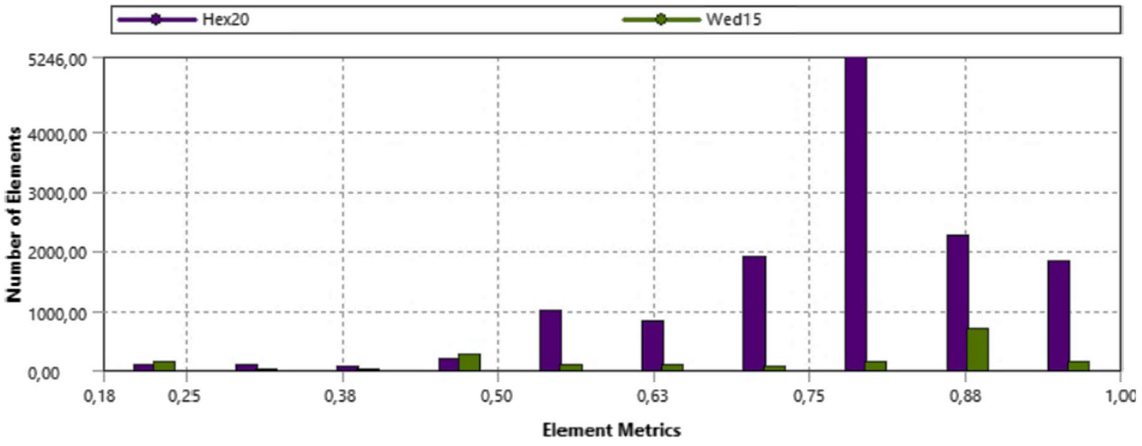

Fig. 10 Mesh quality for the model of 80% infill density

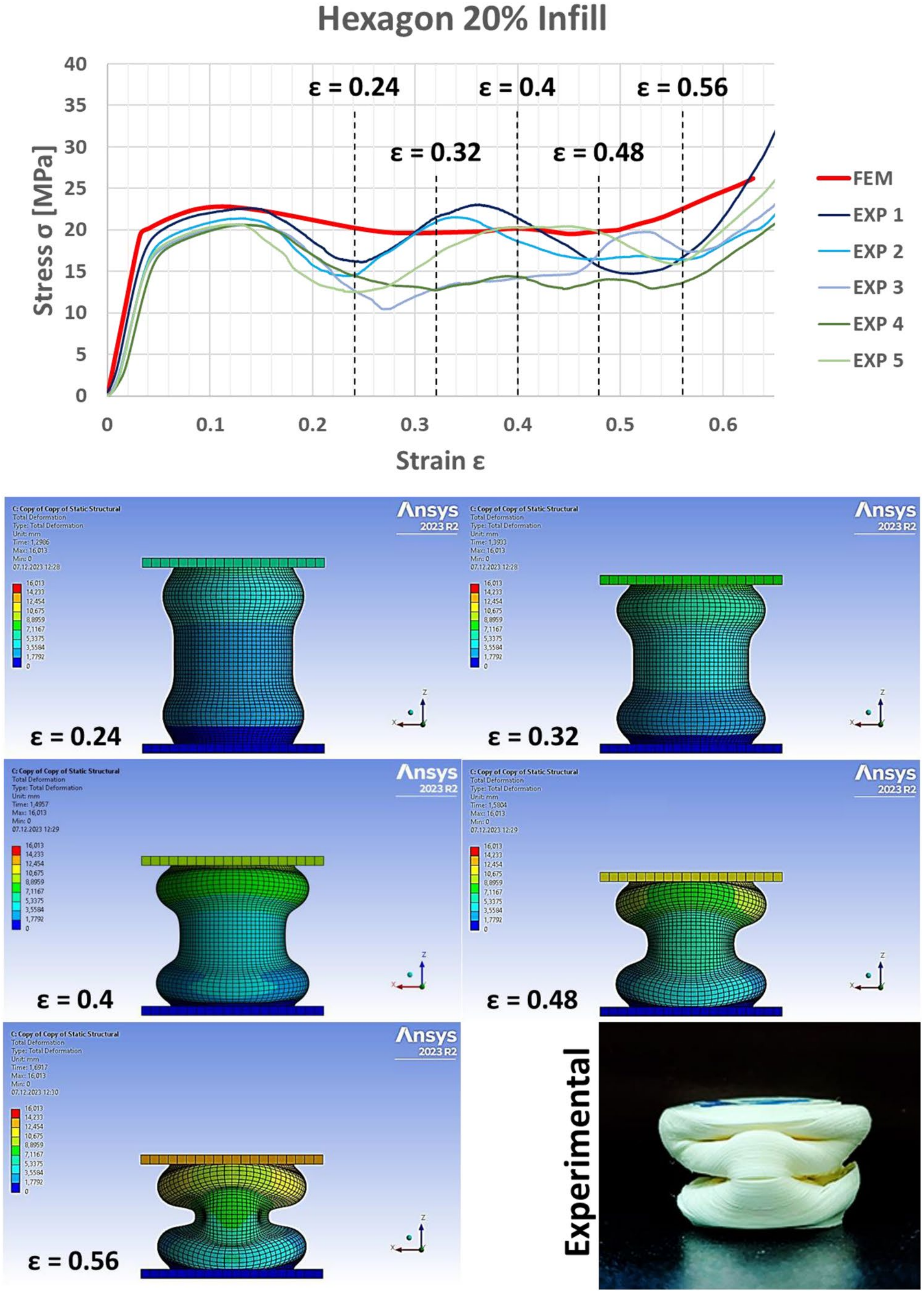

Fig. 12 Stress–strain curve from the compression tests and simulation, with indicative images of the deformed specimen

compression test and its values, despite the complexity of this case, given the formation of characteristic lobes, as it will be afterwards explained.

Apart from the presentation and analysis of the force–displacement results, in order to further exhibit the appropriateness of the developed model, several indicative snapshots for the simulated case of 20% infill percentage of ASA are depicted in Fig. 12, along with the stress–strain curves from both simulation and experiments. As the infill density for this test specimen is rather low, considerable deformation occurs even from the earliest stages of compression, with two almost symmetrical lobes being progressively formed near the upper and the bottom plate, respectively. Finally, when the test is stopped, the deformed specimen mainly consists of the two formed lobes and a small region at the center of the specimen. When this image is compared to the image of a deformed specimen from the experiments, the similarity between the predicted and experimental deformed specimens proves the validity of the proposed model. In general, the mode of deformation of the specimen in this case seems closer to the behavior of thin-walled tubes rather than a solid specimen, given that the core of the specimen is mostly void and the main part of the specimen which withstands the applied loads is actually the wall. More specifically, when the specimen is subjected to compressive loading, the stress distribution becomes non-uniform with higher stresses concentrated in the regions which are in contact with the upper plate of the testing machine. Thus, when the material is deformed, lobes are formed, influenced by the ratio of the specimen diameter to the wall thickness.

In the case of the specimen with an infill density of 50%, an additional amount of material is included than the previous case, leading to a higher force obtained, as can be seen in Fig. 13. In that case, the proposed model can fairly accurately predict the force–displacement curve, at least up to almost 6 mm of displacement, and then, although the shape of the curve is generally similar to some of the experimental curves, the predicted force values are higher, until eventually the difference between the experimental and predicted curves is again reduce at higher values of displacement. The observed discrepancies between the experimental and predicted curves can be attributed to various factors of the proposed model including the material model, geometrical inaccuracies of the produced specimens, and parameters which were not modeled explicitly such as the layer height. However, the proposed model showed a considerable level of realism, as will be afterwards justified based on the observation of the different stages of deformation during the compression test.

As in the case of the specimen with 20% infill density, several snapshots of the simulated compression test were also obtained in the case of the specimen with 50% infill density, depicted in Fig. 14, in order to further investigate the compressive behavior of the ASA specimen. In this case, although from the earliest stages of the deformation, there is a tendency for lobe formation near the two ends of the specimen, the existence of a higher amount of material hinders the clear formation of the lobes as in the previous case. Thus, at the final stage of the compression test, although the shape of the deformed specimen demonstrates that two areas of higher diameter are formed above and below the central region of the specimen, the reduction of diameter in the central region and the curvature of the lobes are much lower, in comparison to the deformed shape of the previous case. These observations closely match the actual shape of the deformed test specimen.

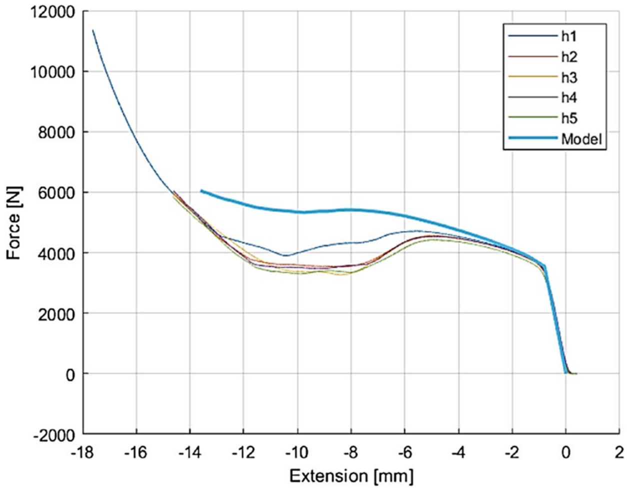

Fig. 13 Comparison of simulation and experimental results regarding the force-extension curve

In the case of the specimen with an infill density of 80%, the volume of voids in the specimen is considerably small, and thus, the material is expected to behave in a way more similar to a solid material, rather than a porous one as in the previous two cases. At first, this is confirmed by the force–displacement curves of Fig. 15, due to the much higher force developed in comparison to the previous two cases. Moreover, the shape of the curve resembles to that of open-die forging with a steep monotonic rise of force as the displacement increases. Although the predicted force–displacement curve generally exhibits a similar behavior to most of the experimental curves during the elastic deformation and initial stages after yield, larger errors occur for displacement values between 6 and 10 mm, and finally, both experimental and predicted curves have the same shape, although the simulation results overestimate the force values. These differences can be attributed to the higher complexity of the specimen geometry, in conjunction with possible defects on the printed specimens, which cannot be explicitly modeled. However, it is proven that the proposed model can provide a precise depiction of the deformation stages of the compression test specimen, according to the experimental test, as will be afterwards discussed in respect to the deformed shape images of the test specimen.

The observations on the snapshots of the simulation of the compression test for the specimen with an infill density of 80% in Fig. 16 justify the previous assumptions, as it becomes evident that the behavior of this test specimen is more similar to the behavior of a solid specimen rather than the porous FFF-printed specimens of the previous cases. The existence of a higher amount of material leads eventually to the barreling phenomenon, by the formation of a barrel-like deformed test specimen due to the friction between the plates and the test specimen, as it was expected in the case of an open die forging, rather than the lobe formation which was observed in cases with lower infill density, when the specimens were similar to thin-walled tubes, something that is verified in comparison to the shape of the actual deformed specimen.

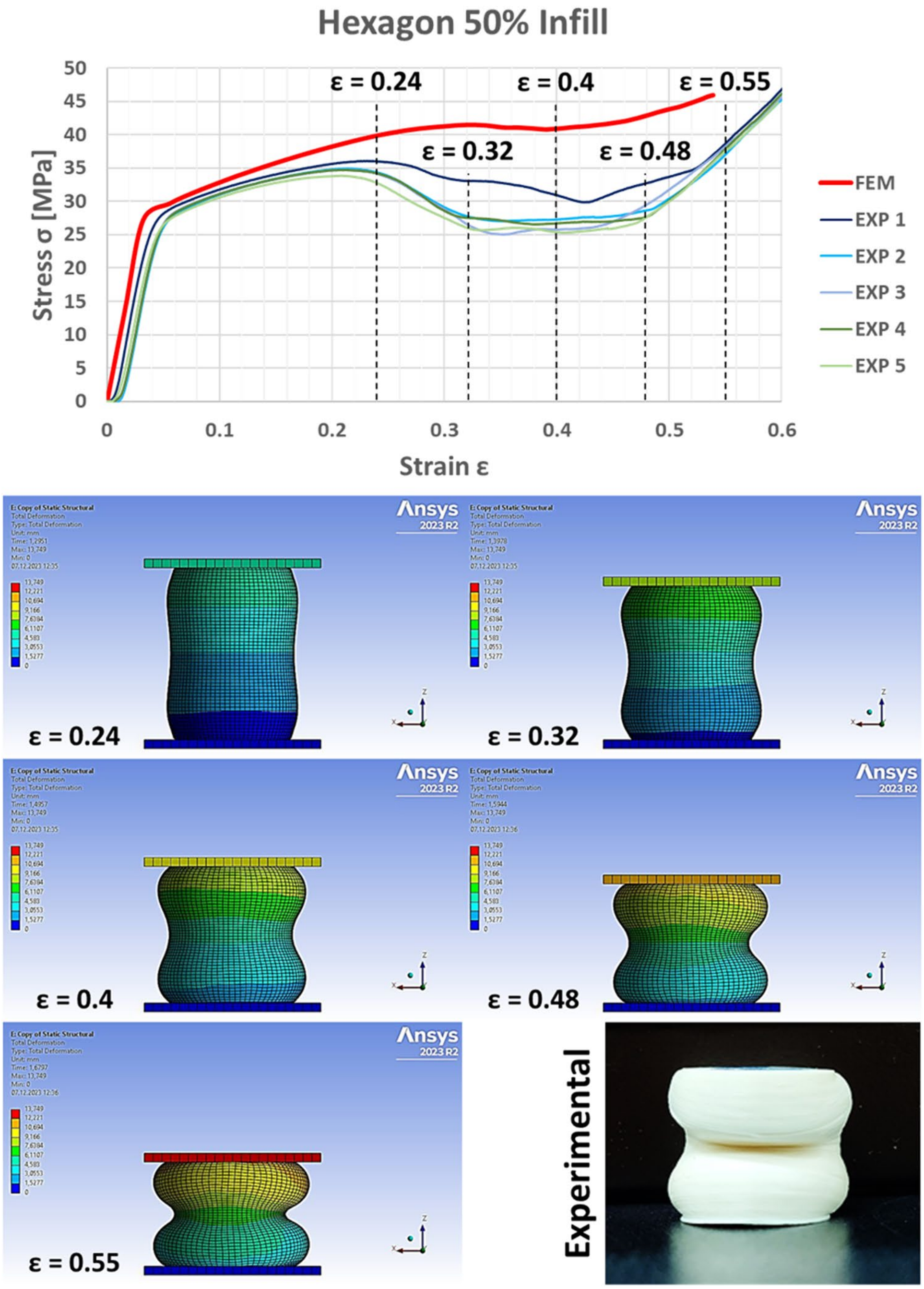

Fig. 14 Stress–strain curve from the compression tests and simulation, with indicative images of the deformed specimen

3.3 Additional simulations results

In order to further assess the validity of the proposed model, additional experimental test cases were carried out and analyzed and the respective simulations were also performed. These cases include compression tests under different infill densities such as 35 and 65%, as well as the extreme case of 0% infill density, where actually the test specimen is only composed of walls with a geometry resembling to that of a thin-walled tube.

After the appropriate mesh size was determined in each case, based on the exact geometry of the test specimens, shown in Fig. 17, the relevant simulations were carried out. In the case of the specimens with 0% infill density, the specimen is actually a thin tube with thin-walled top and bottom surfaces. Thus, its behavior is expected to be relevant to the behavior of compressed thin tubes. The force–displacement curve obtained from the numerical model, presented in Fig. 18, exhibits an almost identical trend at the first stages of compression, as it is very close to the experimental curves

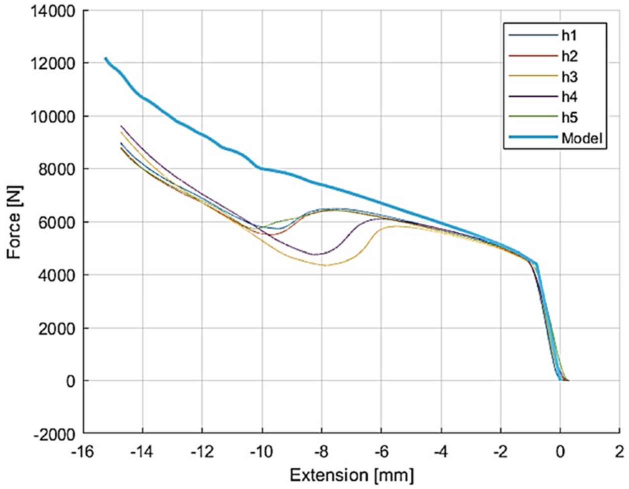

Fig. 15 Comparison of simulation and experimental results regarding the force-extension curve

up to the regions of yield, then it exhibits higher force values up to 7 mm of displacement, and finally, the values lie towards the lowest limits of experimental values but are still consistent with most of the experimental curves.

This behavior of the test specimen is absolutely justified, as the formation of lobes, associated with a non-monotonic increase of force, is an anticipated characteristic of thin-walled tubes. The obtained results from the numerical model exhibit a high degree of accordance with the experimental ones as the predicted force-extension values lie between the lower and higher limit of the experimental curves during most stages of the compression test, thus proving that this approach is able to provide reliable results.

In the case of infill density value of 35%, the accuracy of the numerical model is still considerably high, as can be seen from Fig. 19. More specifically, similar to the case with infill density value of 20%, the predicted force–displacement curve for the compression test of the ASA sample is very close to the experimental curves during the early stages of elastic and plastic deformation, and for displacement values over 7 mm, it lies between the experimental curves, indicating a rather consistent trend with most of them. These observations clearly demonstrate the high reliability of the numerical model regarding the compressive behavior of ASA samples, as it is shown that it can predict the expected mechanical behavior sufficiently during all the stages of deformation.

Finally, the results obtained from experimental tests and numerical simulations for the compression test of ASA samples with 65% infill density are shown in Fig. 20. In this figure, it can be clearly observed that apart from the initial region of elastic deformation and yield, the predicted curve deviates from the experimental results to a higher degree than in the previous cases, especially after 10 mm of displacement. These results indicate that the numerical model, showing a monotonic increase of force after the yield region, predicts a compressive behavior closer to that of a solid specimen rather than a specimen with voids, which is expected to exhibit lower force values during intermediate stages of deformation. These deviations can be attributed to the potential formation of defect structures in the actual specimens and discrepancies of the printing process due to the more complex geometry of the specimens with higher infill density, which cannot be directly modeled and limitations of the numerical approach which was adopted. However, these results are still important as a reference for further studies regarding the behavior of additively manufactured parts.

Based on the results analyzed and discussed in Sections 3.2 and 3.3, a sufficiently deep insight can be obtained into the capabilities and limitations of the FE model regarding the prediction of the compressive behavior of additively manufactured specimens. It is considered important to note that the adopted modeling approach can be efficiently applied for the cases with infill density up to 65%, whereas for higher infill density values, this model consistently exhibits a trend for gradually increasing deviations from the experimental results, mainly showing a higher resemblance to the trend of a solid specimen, rather than the behavior of specimens with voids. For that reason, in the near future, modifications will be carried out in the model in order to be able to predict the compressive behavior even in cases with more complex geometry of the additively manufactured parts such as the ones in the range of infill density values of 65–80%.

4 Conclusions

In the present work, realistic numerical models, taking into account the exact geometry of compression specimens, were developed for the simulation of the compression behavior of ASA polymer specimens fabricated by FFF additive manufacturing. Cases of printed specimens with honeycomb IP and with different infill density values were simulated by finite element models, and after the models were validated by direct comparison to the experimental results, various useful conclusions were drawn.

- The use of the appropriate mesh size leads not only to increased precision but also increases the stability of the numerical simulation of the compression test, as it was found in every case. When the suitable mesh size was employed, the simulation could be carried out without stability issues, regardless of the level of deformation of the simulated test specimens or their geometry.

Fig. 16 Stress–strain curve from the compression tests and simulation, with indicative images of the deformed specimen

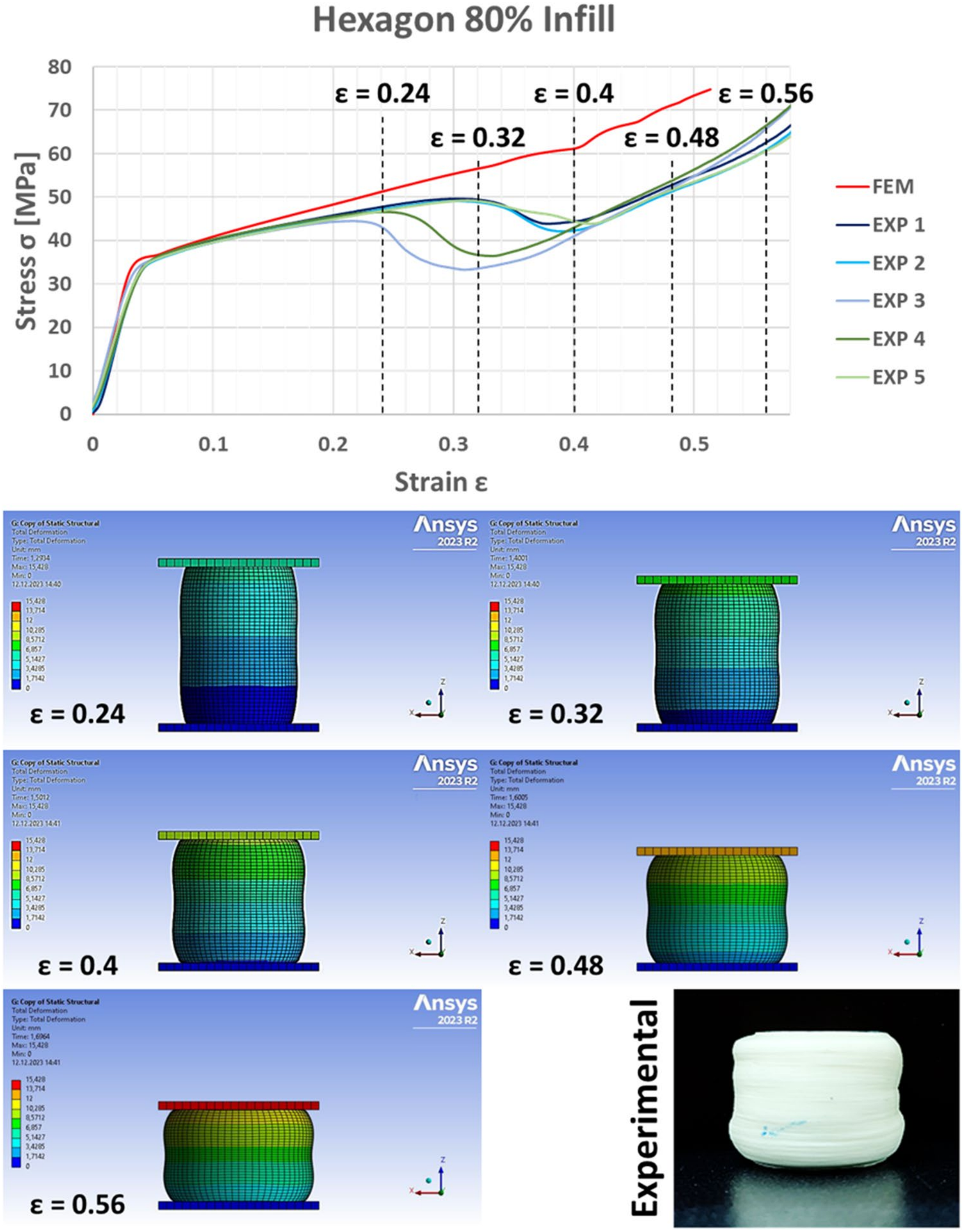

- The proposed finite element model can accurately model the different stages of the deformation of the test specimen with 20% infill density. Although the accuracy becomes lower after the region related to the yield, the simulated results closely match the experimental ones and are able to accurately predict the procedure of lobe formation on the deformed specimen due to its lower density in the core region.
- The accuracy of the proposed model in the case of the model with 50% infill density can be also regarded as acceptable, as it can simulate the shape of the force–displacement curve although the level of accuracy becomes gradually lower for higher displacement values probably due to the material model, unmodeled factors, and defects occurring during the printing process or the experimental test. However, the deformed shape can be realistically predicted based on the model.
- In the last case, involving a test specimen with a high infill density, the model accurately predicts a different behavior than the two previous cases, leading to barreling phenomenon and a different shape of the force–displacement curve. Despite the differences in the predicted loads by the proposed model, its capabilities are shown to be rather high, compared qualitatively to the experimental results both regarding the force–displacement curve and deformed test specimen.
- Experimental and numerical studies on additional cases, such as the ones with infill density values of 0, 35, and

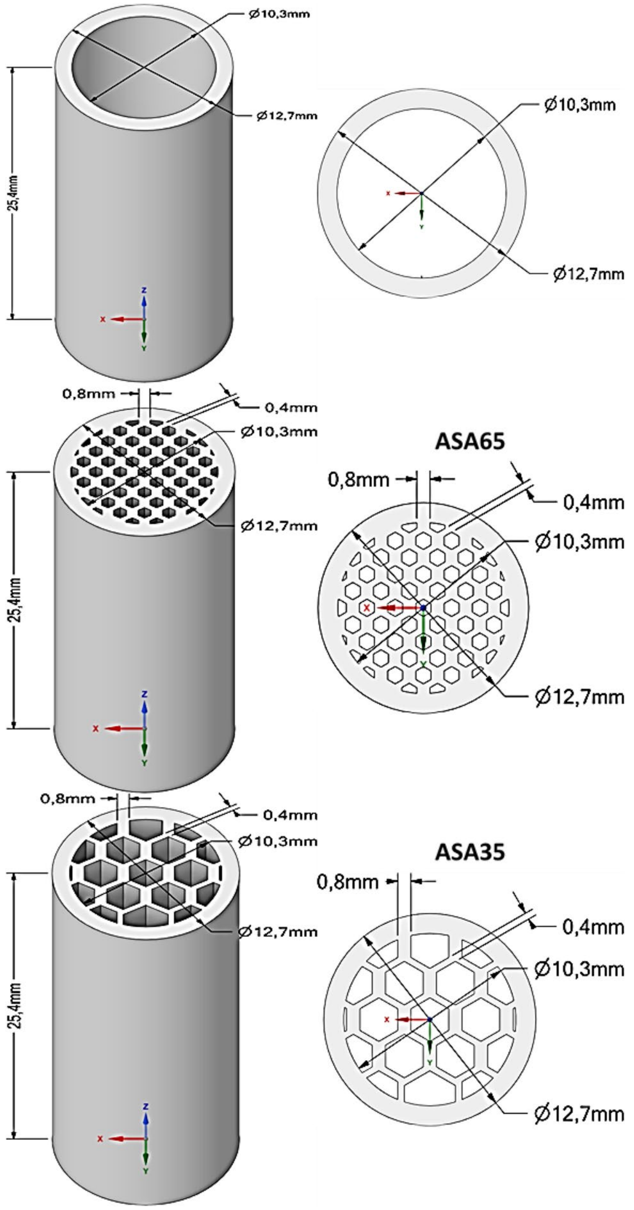

Fig. 17 Test specimen geometry used in the computational model for the additional simulations: **a** 0% infill density, **b** 65% infill density, **c** 35% infill density

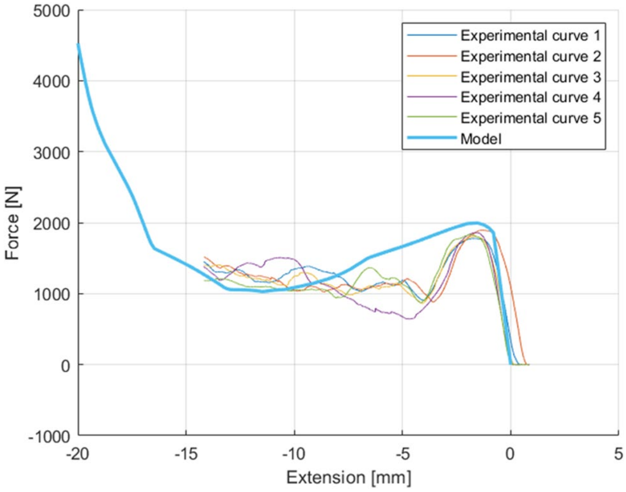

Fig. 18 Comparison of simulation and experimental results regarding the force-extension curve for 0% infill density

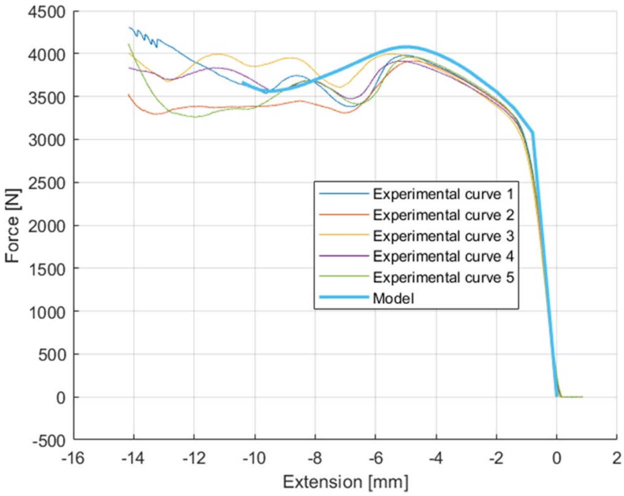

Fig. 19 Comparison of simulation and experimental results regarding the force-extension curve for 35% infill density

65%, further demonstrated the capabilities of the proposed model, indicating that its accuracy is sufficiently high for infill density up to 65% and then, the accuracy is reduced for higher percentages, especially over 65% due to several reasons related to the complexity of the geometry of these specimens. However, this limitation of the proposed model can be addressed in a future study by adopting a more advanced modeling strategy and including details such as the layer height in the FE model.

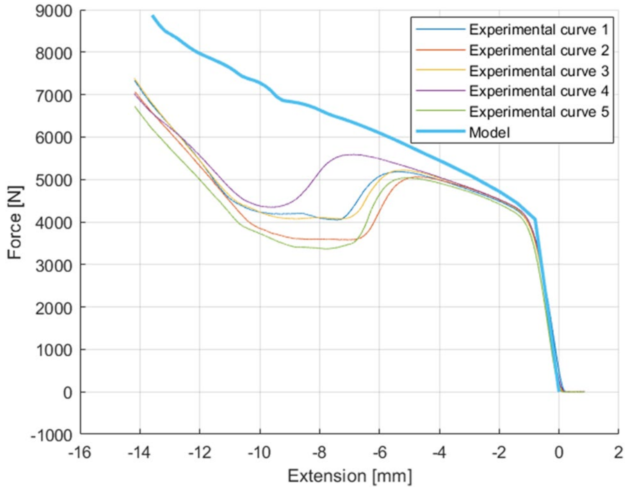

Fig. 20 Comparison of simulation and experimental results regarding the force-extension curve for 65% infill density

Declarations

Ethical approval This article does not contain any studies with human participants or animals performed by any of the authors.

Consent to participate Not applicable.

Conflict of interest The authors declare no competing interests.

References

1. Nadagouda MN, Ginn M, Rastogi V (2020) A review of 3D printing techniques for environmental applications. Curr Opin Chem Eng 28:173–178. https://doi.org/10.1016/j.coche.2020.08.002. ISSN 2211-3398
2. Wang X, Jiang M, Zhou Z, Gou J, Hui D (2017) 3D printing of polymer matrix composites: a review and prospective. Compos Part B: Eng 110:442–458. https://doi.org/10.1016/j.compositesb.2016.11.034. ISSN 1359-8368
3. Hmeidat NS, Kemp JW, Compton BG (2018) High-strength epoxy nanocomposites for 3D printing. Compos Sci Technol 160:9–20. https://doi.org/10.1016/j.compscitech.2018.03.008. ISSN 0266-3538
4. Xu C, Dai G, Hong Y (2019) Recent advances in high-strength and elastic hydrogels for 3D printing in biomedical applications. Acta Biomaterial 95:50–59. https://doi.org/10.1016/j.actbio.2019.05.032. ISSN 1742-7061
5. Karakurt I, Lin L (2020) 3D printing technologies: techniques, materials, and post-processing. Curr Opin Chem Eng 28:134–143. https://doi.org/10.1016/j.coche.2020.04.001. ISSN 2211-3398
6. Pernet B, Nagel JK, Zhang H (2022) Compressive strength assessment of 3D printing infill patterns. Procedia CIRP 105:682–687. https://doi.org/10.1016/j.procir.2022.02.114. ISSN 2212-8271
7. Bonada J, Pastor MM, Buj-Corral I (2021) Influence of infill pattern on the elastic mechanical properties of fused filament fabrication (FFF) parts through experimental tests and numerical analyses. Materials 14(18):5459. https://doi.org/10.3390/ma14185459
8. Lubombo C, Huneault MA (2018) Effect of infill patterns on the mechanical performance of lightweight 3D-printed cellular PLA parts. Mater Today Commun 17:214–228. https://doi.org/10.1016/j.mtcomm.2018.09.017. ISSN 2352-4928
9. Torres J, Cole M, Owji A, DeMastry Z, Gordon A (2016) An approach for mechanical property optimization of fused deposition modeling with polylactic acid via design of experiments. Rapid Prototyp J 22:387–404. https://doi.org/10.1108/RPJ-07-2014-0083
10. ASTM International (2012) Standard terminology for additive manufacturing technologies: Designation F2792–12a. ASTM International, West Conshohocken
11. ISO/ASTM 52920:2023 (2023) Additive manufacturing—qualification principles—requirements for industrial additive manufacturing processes and production sites. ISO, Geneva
12. Monkova K, Monka PP, Hricová R, Hausnerova B, Knapčíková L (2023) Tensile properties of four types of ABS lattice structures—a comparative study. Polymers 15(20):4090. https://doi.org/10.3390/polym15204090
13. Monkova K, Vasina M, Zaludek M, Monka PP, Tkac J (2021) Mechanical vibration damping and compression properties of a lattice structure. Materials 14(6):1502. https://doi.org/10.3390/ma14061502
14. Hanks B, Berthel J, Frecker M, Simpson TW (2020) Mechanical properties of additively manufactured metal lattice structures: data review and design interface. Additive Manuf 35:101301. https://doi.org/10.1016/j.addma.2020.101301. ISSN 2214-8604
15. Forés-Garriga A, Pérez MA, Gómez-Gras G, Reyes-Pozo G (2020) Role of infill parameters on the mechanical performance and weight reduction of PEI Ultem processed by FFF. Mater Des 193:108810. https://doi.org/10.1016/j.matdes.2020.108810. ISSN 0264-1275
16. Yao Y, Ding C, Aburaia M et al (2021) A 3D weaving infill pattern for fused filament fabrication. Int J Adv Manuf Technol 117:3101–3114. https://doi.org/10.1007/s00170-021-07694-z
17. LaleganiDezaki M, MohdAriffin MKA (2020) The effects of combined infill patterns on mechanical properties in FDM process. Polymers 12(12):2792. https://doi.org/10.3390/polym12122792
18. Provaggi E, Capelli C, Rahmani B, Burriesci G, Kalaskar DM (2019) 3D printing assisted finite element analysis for optimising the manufacturing parameters of a lumbar fusion cage. Mater Des 163:107540. https://doi.org/10.1016/j.matdes.2018.107540. ISSN 0264-1275
19. Moretti M, Rossi A, Senin N (2021) In-process simulation of the extrusion to support optimisation and real-time monitoring in fused filament fabrication. Addit Manuf 38:101817. https://doi.org/10.1016/j.addma.2020.101817. ISSN 2214-8604
20. Mercado-Colmenero JM, Rubio-Paramio MA, la Rubia-Garcia MD et al (2019) A numerical and experimental study of the compression uniaxial properties of PLA manufactured with FDM technology based on product specifications. Int J Adv Manuf Technol 103:1893–1909. https://doi.org/10.1007/s00170-019-03626-0
21. Forés-Garriga A, Gómez-Gras G, Pérez MA (2022) Mechanical performance of additively manufactured lightweight cellular solids: influence of cell pattern and relative density on the printing

time and compression behavior. Mater Des 215:110474. https://doi.org/10.1016/j.matdes.2022.110474. ISSN 0264-1275

22. Soe S, Adams R, Hossain M, Theobald P (2021) Investigating the dynamic compression response of elastomeric, additively manufactured fluid-filled structures via experimental and finite element analyses. Addit Manuf 39:101885. https://doi.org/10.1016/j.addma.2021.101885. ISSN 2214-8604
23. Yang Q, Xu F, Yang Y et al (2021) Numerical study on the dynamic characteristics of water entry of cavity body using two-phase SPH method. Acta Mech Sin 37:1072–1089. https://doi.org/10.1007/s10409-021-01060-8
24. Gonabadi H, Chen Y, Yadav A et al (2022) Investigation of the effect of raster angle, build orientation, and infill density on the elastic response of 3D printed parts using finite element microstructural modeling and homogenization techniques. Int J Adv Manuf Technol 118:1485–1510. https://doi.org/10.1007/s00170-021-07940-4
25. Biswas P, Guessasma S, Li J (2020) Numerical prediction of orthotropic elastic properties of 3D-printed materials using micro-CT and representative volume element. Acta Mech 231:503–516. https://doi.org/10.1007/s00707-019-02544-2
26. Fadeel A, Mian A, Al Rifaie M et al (2019) Effect of vertical strut arrangements on compression characteristics of 3D printed polymer lattice structures: experimental and computational study. J Mater Eng Perform 28:709–716. https://doi.org/10.1007/s11665-018-3810-z
27. Kumar SR, Sridhar S, Venkatraman R, Venkatesan M (2021) Polymer additive manufacturing of ASA structure: influence of printing parameters on mechanical properties. Mater Today: Proc 39(4):1316–1319
28. Paul S (2021) Finite element analysis in fused deposition modeling research: a literature review. Measurement 178:109320
29. Torre R, Brischetto S, Dipietro IR (2021) Buckling developed in 3D printed PLA cuboidal samples under compression: analytical, numerical and experimental investigations. Addit Manuf 38:101790
30. Mercado-Colmenero JM, La Rubia MD, Mata-Garcia E, Rodriguez-Santiago M, Martin-Doñate C (2020) Experimental and numerical analysis for the mechanical characterization of PETG polymers manufactured with FDM technology under pure uniaxial compression stress states for architectural applications. Polymers 12:2202
31. Mercado-Colmenero JM, Martin-Doñate C, Moramarco V, Attolico MA, Renna G, Rodriguez-Santiago M, Casavola C (2020) Mechanical characterization of the plastic material GF-PA6 manufactured using FDM technology for a compression uniaxial stress field via an experimental and numerical analysis. Polymers 12:246
32. Athale M, Park T, Hahnlen R, Pourboghrat F (2022) Experimental characterization and finite element simulation of FDM 3D printed polymer composite tooling for sheet metal stamping. Int J Adv Manuf Technol 121:6973–6989
33. Bandinelli F, Scapin M, Peroni L (2024) Effects of anisotropy and infill pattern on compression properties of 3D printed CFRP: mechanical analysis and elasto-plastic finite element modeling. Rapid Prototyp J 30(11):142–158
34. Garcia-Granada AA (2024) High-compression crash simulations and tests of PLA cubes fabricated using additive manufacturing FDM with a scaling strategy. Computation 12:40
35. Kerekes TW, Lim H, Joe WY, Yun GJ (2019) Characterization of process-deformation/damage property relationship of fused deposition modeling (FDM) 3D-printed specimens. Addit Manuf 25:532–544
36. Bhandari S, Lopez-Anido RA, Wang L, Gardner DJ (2020) Elasto-plastic finite element modeling of short carbon fiber reinforced 3D printed acrylonitrile butadiene styrene composites. JOM 72(1):475–484
37. Pastor-Artigues MM, Roure-Fernández F, Ayento-Gubert X, Bonada-Bo J, Pérez-Guindal E, Buj-Corral I (2020) Elastic asymmetry of PLA material in FDM-printed parts: considerations concerning experimental characterization for use in numerical simulations. Materials 13:15
38. Bol RJM, Šavija B (2023) Micromechanical models for FDM 3D-printed polymers: a review. Polymers 15:4497
39. Gonabadi H, Hosseini SF, Chen Y, Bull S (2024) Size effects of voids on the mechanical properties of 3D printed parts. Int J Adv Manuf Technol 132:5439–5456
40. Bian Y, Yang F, Zhang S, Chen M, Song Y (2022) Similaritites of the mechanical responses of body-centered cubic lattice structures with different constituent materials under compression. JOM 74(4):1774–1783
41. Amirpour M, Battley M (2022) Study of manufacturing defects on compressive deformation of 3D-printed polymeric lattices. Int J Adv Manuf Technol 122:2561–2576
42. Rezaei R, Ravari MRK, Badrossamay M, Kadkhodaei M (2017) Mechanical characterization and finite element modeling of polylactic acid BCC-Z cellular lattice structures fabricated by fused deposition modeling. Proc Inst Mech Eng C J Mech Eng Sci 231(11):1995–2004
43. Ravari MRK, Kadkhodaei M, Badrossamay M, Rezaei R (2014) Numerical investigation on mechanical properties of cellular lattice structures fabricated by fused deposition modeling. Int J Mech Sci 88:154–161
44. Wen Z, Li M (2021) Compressive properties of functionally graded bionic bamboo lattice structures fabricated by FDM. Materials 14:4410
45. Kaveloglu S, Temiz S (2022) An experimental and finite element analysis of 3D printed honeycomb structures under axial compression. Polym Polym Compos 30:096739112211223
46. Sala R, Regondi S, Pugliese R (2022) Design data and finite element analysis of 3D printed poly(ε-caprolactone) -based lattice scaffolds: influence of type of unit cell, porosity, and nozzle diameter on the mechanical behavior. Eng 3:9–23
47. Bru J, Leite M, Ribeiro AR, Reis L, Deus AM, Fátima-Vaz M (2020) Bioinspired structures for core sandwich composites produced by fused deposition modeling. Proc Inst Mech Eng L: J Mater: Des Appl 234(2):379–393
48. Johnston R, Kazanci Z (2021) Analysis of additively manufactured (3D printed) dual-material auxetic structures under compression. Addit Manuf 38:101783
49. Ali MH, Batai S, Karim D (2021) Material minimization in 3D printing with novel hybrid cellular structures. Mater Today: Proc 42:1800–1809
50. Corvi A, Collini L, Sciancalepore C, Kumar A (2023) Analysis and modelling of damage mechanism in FDM 3D-printed lattice structure under compression loading. J Mech Sci Technol 37(3):1089–1095
51. Peng C, Tran P, Mouritz AP (2022) Compression and buckling analysis of 3D printed carbon fibre-reinforced polymer cellular composite structures. Compos Struct 300:116167
52. Podroužek J, Marcon M, Ninčevič K, Wan-Wendner R (2019) Bio-inspired 3D infill patterns for additive manufacturing and structural applications. Materials 12:499
53. Sunny SF, Rostami S, Malik AS (2018) Effects of fluid cavity modeling when predicting compressive strength of FDM printed nylon with varying infill pattern and density, Proceedings of the ASME 2018 13th Manufacturng Science and Engineering Conference MSEC 2018, June 18–22, College Station, TX, USA
54. Sukindar NA, Samsudin NM, Shaharuddin SIS, Kamaruddin S (2022) The effects of FDM printing parameters on the compression properties of polymethylmethacrylate (PMMA) using finite element analysis. Int J Integr Eng 14(2):86–92
55. Guessasma S, Belhabib H, Nouri O (2016) Ben Hassana, Anisotropic damage inferred to 3D printed polymers using fused deposition modeling and subject to severe compression. Eur Polymer J 85:324–340
56. Głuch K, Szot E, Gruszecka A, Szymańska-Chargot M, Cytawa J, Michalak L (2009) Kinetic energy release and mean life time of

metastable ions produced from C3H3N. Vacuum 83(Supplement 1):S20–S23. https://doi.org/10.1016/j.vacuum.2009.01.014. ISSN 0042-207X

57. Ahsanulkabir, Chowdhury MA, Hossain N, Islam MA, Aoyon H, Md. Masud Rana (2023) Graphene reinforced 3D printed polymer nanocomposites for diverse applications. Results Chem 6:101197. ISSN 2211-7156. https://doi.org/10.1016/j.rechem.2023.101197
58. Wu Y, Zhu C, Yanchen Z, Qiu H, Ma H, Gao C, Liu Y (2020) A type of silicone modified styrene-acrylate latex for weatherable coatings with improved mechanical strength and anticorrosive properties. React Funct Polym 148:104484. ISSN 1381-5148.https://doi.org/10.1016/j.reactfunctpolym.2020.104484
59. ASTM D695; Designation: D695—15 (2015) Standard test method for compressive properties of rigid plastics 1. ASTM, West Conshohocken